

# Vessel Visualization with Volume Rendering

Christoph Kubisch, Sylvia Glaßer, Mathias Neugebauer,  
and Bernhard Preim

**Abstract** Volume rendering allows the direct visualization of scanned volume data, and can reveal vessel abnormalities more faithfully. In this overview, we will present a pipeline model for direct volume rendering systems, which focus on vascular structures. We will cover the fields of data pre-processing, classification of the volume via transfer functions, and finally rendering the volume in 2D and 3D. For each stage in the pipeline, different techniques are discussed to support the diagnosis of vascular diseases. Next to various general methods we will present two case studies, in which the systems are optimized for two different medical issues. At the end, we discuss current trends in volume rendering and their implications for vessel visualization.

## 1 Introduction

For the diagnosis of vascular diseases, like stenosis, plaques, and other vessel wall abnormalities, contrast-enhanced image data, such as CT angiography or MR angiography data, are acquired. Direct volume rendering of these datasets is a viable option and complements slice-based viewing. The increased image intensity of the contrast-enhanced vessels is used to selectively emphasize them. Compared to threshold-based surface rendering or surface rendering of segmentation results, direct volume rendering (DVR) represents vascular structures, in particular small vessel abnormalities, more faithfully. This is achieved by avoiding the binary decision, which portions of the data belong to a surface. With carefully refined transfer functions (TF) different portions of the vessel wall, e.g. arease with plaque

---

C. Kubisch (✉) · S. Glaßer · M. Neugebauer · B. Preim  
Institute of Simulation and Graphics, University of Magdeburg  
e-mail: [kubisch@isg.cs.uni-magdeburg.de](mailto:kubisch@isg.cs.uni-magdeburg.de); [glasser@isg.cs.uni-magdeburg.de](mailto:glasser@isg.cs.uni-magdeburg.de);  
[neugebauer@isg.cs.uni-magdeburg.de](mailto:neugebauer@isg.cs.uni-magdeburg.de); [preim@isg.cs.uni-magdeburg.de](mailto:preim@isg.cs.uni-magdeburg.de)

are displayed. A survey of surface-based vessel visualization techniques with applications in treatment planning and surgical training was presented in [1]. In contrast, this chapter is focussed on volume rendering and consequently diagnostic applications.

*Data Quality.* Ideally, the contrast agent is equally distributed in all vascular structures which are relevant for diagnosis. In clinical practice, the contrast agent spreads with a certain speed and thus cannot reach a complete vascular tree at a particular point in time. Moreover, the contrast agent diffuses in the surrounding and leads to (again irregularly) increased image intensity values. The non-uniform spatial distribution of the contrast agent is referred to as contrast agent inhomogeneity. A simple technique to compensate for this artefact is a so called background compensation [2], which estimates the different background values and adaptively corrects them.

Another general problem is the small scale of vascular structures. A large portion of the voxels belonging to a blood vessel are boundary voxels. These voxels comprise vessel portions and portions of other tissues resulting in a state that is generally referred to as the *partial volume effect*. This leads to an averaging of the image intensities. As a consequence, small side branches of vascular structures may be hidden and larger branches may appear smaller than they actually are.

Finally, the image intensity of contrast-enhanced vascular structures in CT data is in the same range as bony structures. In some regions of the body, these bony structures may be far away from the vascular structures and can be efficiently removed by applying clipping planes. However, in other regions, such as the skull, this is often not feasible due to a close neighborhood.

The remainder of this chapter is organized as follows. We describe a vessel visualization pipeline in Sec. 2. We go on and discuss the elements of that pipeline, namely data preprocessing (Sec. 3), classification (Sec. 4), and rendering (Sec. 5). Case studies, where the general principles are applied to specific diagnostic tasks, are presented in Sec. 6.

## 2 Vessel Visualization Pipeline

We define the visualization of vessels from volume data as a pipeline process. The common goal of this pipeline is to support the diagnosis of vascular diseases, such as stenoses (narrowings), aneurysms, and plaque formations. This goal is achieved by the use of isolated views and focus-and-context visualizations. The focus can be the vessels themselves, pathologic portions of a vessel, or their spatial relationship to other organs. The context is mostly provided by the surrounding tissue, which aids therapy planing by providing functional relationships. We will present the following stages of the pipeline:

1. *Data Preprocessing:* Additional anatomic structures next to the volume data are identified and delineated to aid the vessel identification. The volume may be filtered for noise removal.

2. *Classification with Transfer Functions*: The intensity values stored in the volume are mapped to optical properties, like color and opacity values.
3. *Rendering*: The volume data is rendered as 2D or 3D image and might be limited to single vessel paths.

Common visualization goals are the removal of obstructing tissue and highlighting vessel pathologies. When it comes to intervention planning, surrounding context structures gain more importance. The presented DVR pipeline focuses more on the vessels themselves.

### 3 Data Preprocessing

In a first stage, various preprocessing steps on the volume data can be carried out. Initially, filtering techniques may remove noise or compensate for contrast agent inhomogeneity [3]. Bone removal (Sect. 3.1), vessel segmentation (Sect. 3.2), and emphasis of elongated vessel-like structures (Sect. 3.3) are frequently performed to display the vessels. These methods can strongly improve the visual quality, since vessels are relative small structures inside the volume and thus can be easily obstructed.

#### 3.1 Bone Removal

In most regions of the human body, (contrast-enhanced) vascular structures and skeletal structures cannot be discriminated reliably [4]. Bone removal is part of almost all modern radiology workstations. In most cases, it is sufficient if the user marks a connected skeletal component with one click of a pointing device to initiate a (more or less advanced) region growing method to roughly segment this structure (see Fig. 1).

#### 3.2 Vessel Segmentation

Another common task is the segmentation of the vessel voxels. The segmentation of vascular structures allows to adjust a TF to the image intensities, in particular to the histogram of vessel voxels. This is essential since they occupy only a small fraction of the entire dataset ( $\approx 2\text{-}5\%$  in the coronary datasets used in Sect. 6.2) and thus are hardly recognizable in the global histogram. There exist various segmentation techniques. The conceptually most simple method is *region growing* [5]. From an initial set of seed points, more and more neighboring image voxels are included as long as they can be classified as vessels. Typically, this inclusion is bound to a global intensity threshold. The progressing boundary of the segmentation process can also

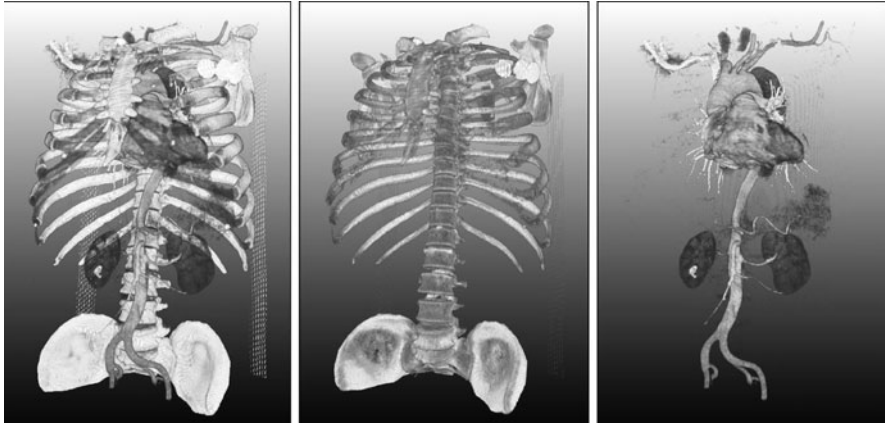


**Fig. 1** DVR of vascular structures. Original scene (left), bones to be removed (middle) and resulting visualization restricted to the heart, the kidney and vascular structures (right). Compared to the initial scene, bone removal significantly improves the display of vascular structures. (Image courtesy of Johann Drexl, Florian Link and Horst Hahn, Fraunhofer MEVIS)

be interpreted as wave front that propagates through the segmented object. This interpretation forms the basis of the *level set* and *fast marching* methods [6]. Local image features, such as intensities, gradients, and textures, control this propagation adaptively. Therefore, the front is rapidly moved towards those regions, which are likely part of the vascular system, and is hindered from others.

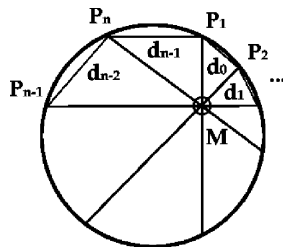
After segmentation, the centerlines of vessels and the whole vessel tree can be extracted through *skeletonization*. This can be achieved by basic operations, which commonly use *thinning* to create a single voxel wide representation of the vessel tree. Thinning can be implemented by the morphological operator *erosion*, which has to consider the anisotropic character of medical image data (slice distances are usually larger than in-plane resolution). The centerline can be used for vessel specific rendering techniques (see Sect. 5.2) or for the analysis of vessel attributes, such as the diameter.

A variation of segmentation is *vessel tracking*, in which a path along the vessel is extracted from a given starting point. Various methods exist, some extract single paths, others can locate the entire vessel tree and correctly handle vessel branching. At the *Rotterdam Coronary Artery Algorithm Evaluation Framework* [7] many methods have been compared and analyzed with respect to accuracy, speed, and level of user interaction. For more details on vessel segmentation and skeletonization, we refer to Boskamp et al. [8].

### 3.2.1 Centerline Correction

An initial vessel path can be refined, so that it reflects the centerline more accurately. For each pathpoint  $M$ , a tangential plane  $T$  is generated, in which the point is moved

**Fig. 2** The original center  $M$  is corrected by a weighted sum of the radial hitpoints  $P_i$  and the distances  $d_i$  between them



towards the center [9]. The center is approximated by casting radial rays within the plane, which generate a series of hitpoints  $P_i$  with the vessel wall (see Fig. 2). The hitpoint generation requires pre-defined thresholds for the vessel's inner and outer intensities. The distances  $d_i$  between adjacent hitpoints are used to approximate a new center point  $N$ :

$$N \approx \frac{\sum_{i=1}^n P_i \cdot (d_{i-1} + d_{(i) \bmod n})}{2 \cdot \sum_{i=0}^{n-1} d_i} \quad (1)$$

As vessels typically exhibit smooth curvature and no abrupt changes in flow, spline-interpolated pathpoints and tangents can be used. This is particularly useful when the segmentation yields a path with discrete voxel coordinates.

### 3.3 Filtering

Similar to segmentation, it is also possible to find voxels that are usually part of vessels with filtering, since they exhibit certain geometric features in their neighborhood. Whilst segmentation classifies voxels in a binary fashion, filtering assigns real probability values to each voxel, the *vesselness* factor. This factor is mostly related to finding elongated round structures. Filtering uses the local neighborhood of each voxel and treats all voxels in the same manner. Detection of the vesselness is challenging, because especially at branchings, the local neighborhood does not reveal elongated structures.

To compute the vesselness, Frangi et al. [10] used the Hessian matrix  $\mathcal{H}$  to detect tubular structures. A common approach to analyze the local behavior of an image  $L$  is to consider its Taylor expansion in the neighborhood of a point  $x_o$ :

$$L(x_o + \delta x_o, s) \approx L(x_o, s) + \delta x_o^T \nabla_{o,s} + \delta x_o^T \mathcal{H}_{o,s} \delta x_o \quad (2)$$

This expansion approximates the structure of the image up to the second order.  $\nabla_{o,s}$  and  $\mathcal{H}_{o,s}$  are the gradient vector and the Hessian matrix of the image computed in  $x_o$  at scale  $s$ . Varying  $s$  will represent different vessel diameters, and the results

of each filter run are combined using the maximum in the end. To calculate these differential operators of  $L$ , convolution with derivatives of Gaussians are used. Analysis of the second order derivatives information (Hessian) has an intuitive justification in the context of vessel detection. The second derivative of a Gaussian kernel at scale  $s$  generates a probe kernel that measures the contrast between the regions inside and outside the range  $(-s, s)$  in the direction of the derivative.

At the core of the vessel filter lies an eigenvector decomposition of the Hessian matrix, which describes the local principal directions of the curvature. Given the 3D volume space, this yields three orthonormal vectors  $(\lambda_1, \lambda_2, \lambda_3)$  due to the matrix's symmetry. The eigenvector with the smallest absolute eigenvalue corresponds to the direction that represents the least curvature, i.e. along the vessel direction. If the vectors are sorted by their magnitude  $(|\lambda_1| < |\lambda_2| < |\lambda_3|)$ , an ideal tubular structure in a 3D image would have the following attributes:

$$|\lambda_1| \approx 0 \quad (3)$$

$$|\lambda_1| \ll |\lambda_2| \quad (4)$$

$$|\lambda_2| \approx |\lambda_3| \quad (5)$$

These attributes only describe cylindrical structures, which means they are inappropriate at vessel branchings. The final vesselness is a product of different parameters that represent geometric details such as blob-like structures or plane- and line-like patterns. To refine the result, the user can control these parameters, which are based on the  $\lambda$  vectors, by custom weights. One of the parameters takes the intensity values into account to lower the impact of noisy background values. For further details on the entire filter construction, we refer to [10].

Because the vesselness is only defined for a single diameter, a multi-scale approach is employed. Since only tubular structures are determined by this filter, the detection of vessels in branching areas leaves room for improvement. The multi-scale approach is also limited in dealing with varying vessel diameters, due to its limitation to fixed diameters. These issues were dealt with by Joshi et al. [11], who used a mix of Hessian- and entropy-based filtering. Their entropy factor was generated from analyzing the polar profiles of each voxel. Figure 3 depicts such a profile in the 3D case. For each direction, the variance in intensities and average intensity are computed within the neighborhood. The likelihood of clusters within such profiles is used to calculate the vesselness.

Compared to the hessian-based technique, the profiles do not require multiple runs for different vessel diameters and especially the quality around branching points has been improved (see Fig. 4). However, the method's implementation in Matlab on a 3.2 GHz Pentium IV is very time-consuming, i.e. it resulted in a four hour computation, which is unfavorable in the clinical routine. With the use of per-voxel factors, either probability-based or binary from segmentation, the later rendering of volumetric vessel data is reduced or highlighted to the important vascular structures.

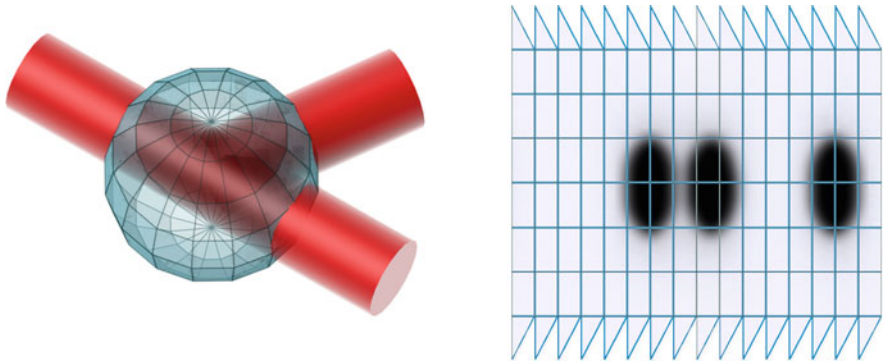


**Fig. 3** A spherical profile (right) for branching vessels (left). The profile shows a phantom distribution of the intensities on the spherical map for a single radius. By using multiple radii the mean value intensities and variance of intensities along each solid angle can be derived. A cluster analysis on this data is used to contribute to the vesselness factor

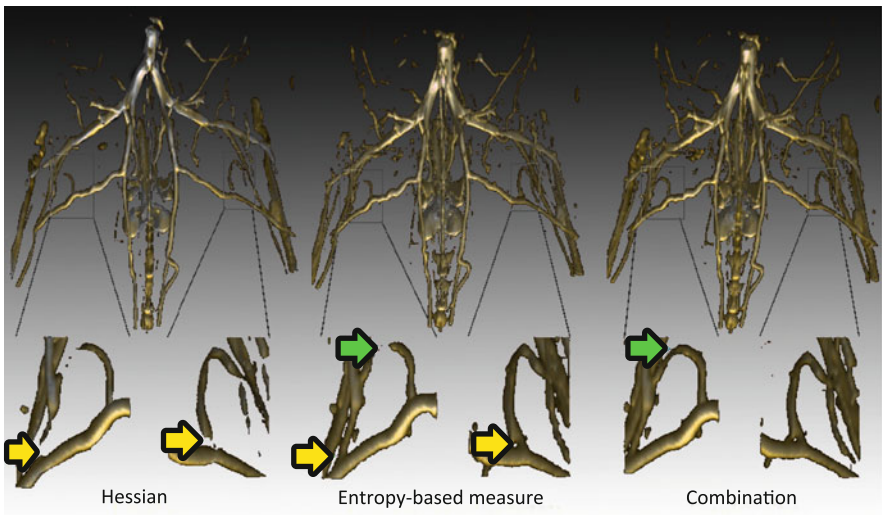


**Fig. 4** Comparison of the Hessian-based (left) and entropy-based (middle), polar profile, vessel filters. The green arrows mark benefits of the earlier method, and the yellow arrows show improvements of the latter. The final (right) image shows a combination of both techniques. Image from [11]

### 4 Classification with Transfer Functions

Segmented data provides additional information, that can aid analysis of the volume data for classification. DVR requires a classification  $C$  of the measured intensity value  $i$ , which maps intensity values to colors and opacities:

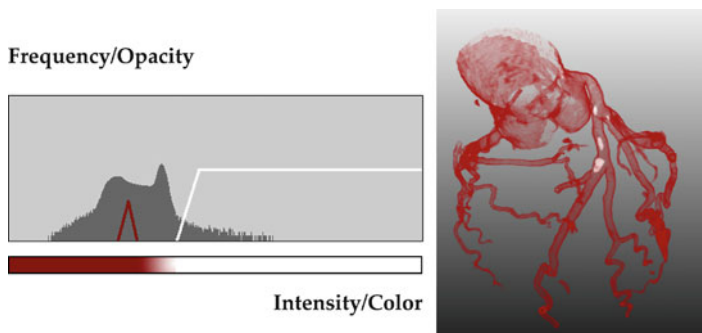


**Fig. 5** TF specification with a piecewise linear function to emphasize two tissue types. The histogram is shown as context. The supporting points of the 1D transfer function can be arranged (left) to highlight only focus structures (right), in this case calcified plaques within the segmented coronary vessels

$$C(i) \rightarrow (r, g, b, \alpha) \quad (6)$$

This can be used to color-code anatomical structures differently and make them invisible or transparent. For faster processing, the classification is often pre-computed and encoded into lookup-textures. It can be applied to each voxel before rendering (*pre-classification*), or during runtime sampling (*post-classification*). The latter yields much higher quality, because the interpolated intensity values between voxels are classified on their own.

A piecewise linear function can be defined through multiple supporting points that highlight certain intensity ranges and hide others (see Fig. 5). If the objects lie within certain intensity ranges, the histogram information aids the manual specification process.

The classification may not only depend on the intensity values. Kindlmann and Durkin [12] have shown how *multi-dimensional TFs (MDTF)* can be semi-automatically generated in order to emphasize transitions between materials. To discriminate values with the same intensity, additional attributes are taken into account. One typical attribute is the gradient magnitude: homogenous regions have a small gradient and larger gradients can be found at tissue transitions. With a higher-dimensional domain, the TF design process itself becomes harder, as arbitrary shapes and color gradients can now be used to classify the regions of interest in the multi-dimensional space. Several ways to deal with this complexity exist, either by automatizing the process, or by supporting the manual process through appropriate user interfaces [13].

In principle, MDTF allows to display vascular and skeletal structures simultaneously, as well as to discriminate them e.g. by using different colors, which was not possible with 1D TFs. Thus, expressive visualizations of complex spatial relations may be achieved, e.g. blood vessels close to the cranium [14] (see Fig. 6, where image intensity and gradient magnitude are employed).



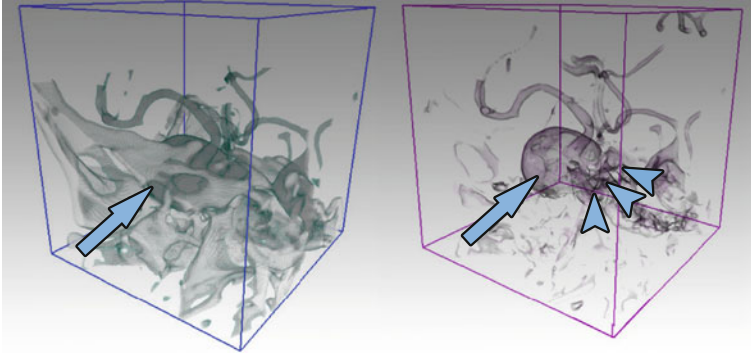


**Fig. 6** Application of 2D TFs. Additionally to the intensity values in the 1D TF (left) the gradients are used for classification and therefore improve the image quality (right). The arrow shows the aneurysm, while the arrowheads point to the parent arteries, which were obstructed by skull tissue. Image from [14]

#### 4.1 Histogram Analysis for Transfer Functions

A histogram analysis can automatize the TF specification for emphasizing dataset specific boundaries. Rezk-Salama et al. [15] used this approach for their *implicit segmentation*, in which anatomic structures appear as being (explicitly) segmented. A histogram-based method was also chosen by Vega Higuera et al. [16] to emphasize cerebral vasculature with specification of a 2D TF. The histogram is analyzed for gradient magnitudes and intensity values to only highlight blood vessel walls in datasets for diagnosing intracranial aneurysms (more detail in Sect. 6.1). This automatic method strongly speeds up the process, which otherwise requires a trained expert, due to the small size of the selected region in the 2D histogram. Based on a reference dataset and a reference classification, a non-rigid registration between examined and reference datasets' 2D histograms is performed. The reference TF is then smoothly deformed using bicubic B-Splines to the new dataset. The result of this method works very well and is presented in Fig. 6.

To detect peaks of smaller objects, *local histograms* can be determined in sub-regions, or along lines, also known as intensity profiles. Lundström et al. [17] partition the volume into regional neighborhoods for which they compute histograms. Because a clear visual segmentation is not always possible, animation techniques were introduced to represent the probability of the individual classification [18]. Instead of mixing the overlapping colors for each structure's intensity region, the pure colors are presented in an animated series proportional to their probability. Therefore, the information about the ambiguity is not lost and helps medical doctors becoming aware of uncertainties.

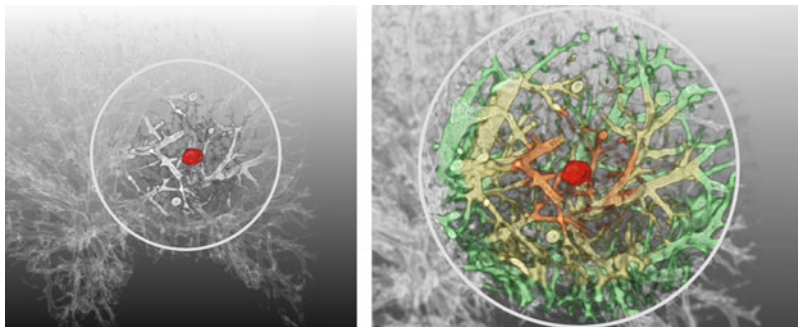


**Fig. 7** Distance-based transfer function applied to abdominal CT data. In the left image the vessels within the security margin around the tumor (red) have higher opacity. In the right image different distance ranges are color-coded. The security margins around tumors are essential to assess operability. Image Courtesy of Andreas Tappenbeck, University of Magdeburg

## 4.2 Spatial Transfer Functions

The distance to focus structures can also be used as input to MDTFs [19] (see Fig. 7). Prior to the application, a distance field for the given key structure needs to be computed, which requires segmentation of that structure. The sign of the voxel in the distance field is used to discriminate between interior and exterior volume.

The local size of regions was used as secondary input to MDTFs by Correa et al. [20]. They did not use a segmentation, but based their relative size metric on a continuous scale-space analysis and a set of detection filters. Their algorithm works in three steps:

1. *Scale-space computation.* The user defines a set of interesting scales (similar to the vessel diameters in Hessian-based filtering in Sect. 3.3). Through forward Euler integration, this scale-field is generated based on diffusion using a custom conductivity function. The result of this process are various scale fields.
2. *Scale detection.* Within the scale fields a point set is created by running detection filters. The points are maxima in space and scale, referred to as Laplacians of Gaussians. In the authors' application, the point set defined spheres, which represent blob structures of various radii.
3. *Backprojection.* The relative size volume is created from the point set by scattered data interpolation. This was accomplished with Shepard's interpolation that uses a fourth-degree Wendland polynomial as common basis function.

In the end, the relative size is used for the classification. The authors have mapped size to color values and a combination of size and intensity to opacity and generated appealing illustrations of the vessels in the *visible human's* hand dataset.

## 5 Rendering

In the rendering stage the classification is finally applied. In medical workstations a combination of 3D and 2D views is used to provide the viewer with different spatial information about the vessels. We will mention some of the principle methods used in this stage. For the spatial context the 3D views, typically generated through ray-casting, are frequently used (Sect. 5.1), whilst reformation (Sect. 5.2) and unfolding techniques (Sect. 5.3) create 2D images for detailed vessel inspection. Kanitsar et al. [21] have performed extensive research on various 2D visualization techniques for diagnostic relevance.

### 5.1 3D View

The 3D view gives an overview of the basic branching pattern of the vascular tree, and – depending on the TF design – it gives clues to context structures surrounding the vessels. A wide-spread DVR option is the Maximum-Intensity Projection (MIP), a rendering mode, where the brightest voxel along each viewing ray is displayed independent from its position in 3D space. Thus, a single MIP image does not convey any depth cues. Therefore, it is essential to rotate such visualizations or to use predefined videos of such rotations in order to benefit from depth-cues resulting from the motion parallax. The image intensity of the selected voxels is usually linearly mapped to the brightness of a gray value. Given the intensities  $I$  along the viewing ray from  $s_{\text{start}}$  to  $s$ , the MIP is simply the maximum of all sampled intensities.

$$\text{MIP}(s) = \max_{s_{\text{start}}}^s(I(\vec{s})) \quad (7)$$

For clinical users, the simplicity of MIP images is a great advantage: No parameter needs to be adjusted and the relation between image intensity in the final image and the underlying data is quite direct. The partial volume effect is often strongly disturbing, because it hides small vascular structures in front of larger vascular structures. As a remedy, the closest vessel projection (CVP) [22], also called Local MIP, has been introduced [23]. With this variant, instead of the global maximum along a viewing ray, the first local maximum above a certain threshold  $t$  is selected. CVP images thus provide correct depth information. However, the user has to specify  $t$  appropriately. As a rule of thumb, a certain percentage of the global maximum intensity of the whole dataset is usually appropriate and “suggested” as default value.

#### 5.1.1 GPU-Ray-Casting

With the advancement of programmable graphics hardware *GPU-ray-casting* has become the state-of-the-art technique also for the visualization of vascular structures.



**Fig. 8** GPU-ray-casting with position buffers applied to coronary vessels in CT data. An approximated mesh hull of the volume is rasterized into ray-start- (left) and ray-end-position (middle) buffer. Both are used for the final volume rendering (right) through a viewport-spanning quad mesh

The approximated calculation of the *volume rendering integral* ( $I$  radiance,  $D$  end position, the radiance  $I_0$  at the background position  $s_0$ ,  $\kappa$  being the absorption and  $q$  being the emission of light):

$$I(D) = I_0 e^{-\int_{s_0}^D \kappa(t) dt} + \int_{s_0}^D q(s) e^{-\int_s^D \kappa(t) dt} ds. \quad (8)$$

can be performed with custom loops in the pixel processing stage of the hardware, substantial flexibility and performance was gained. Scharlach et al. [24] provide a robust setup for perspective and orthogonal ray-casting. It uses acceleration strategies, such as empty space skipping and early ray termination. The key idea is to create two image space buffers for ray start and end positions (see Fig. 8 left and middle), which are used as input for the final pixel processing program. To accelerate empty space skipping, a hull mesh can be created at a coarser resolution than the actual volume. Its positions are rasterized into the ray position buffers. Special care must be taken to avoid artifacts resulting from clipping the hull mesh with the near plane. Empty space skipping is particularly useful, as the vascular structures typically cover only a small subset of the data.

When using *volume splatting*, such as presented by Vega Higuera et al. [25] for displaying neuro-vascular data, empty space skipping can be performed more accurately. As the ray position buffers only store entry and exit positions, the empty area inbetween cannot be encoded. Volume splatting, however, uses particles to approximate the filled parts of the volume. Compared to ray-casting, the splatting comes at the cost of rasterizing many small primitives on their own, creating many context switches for the hardware. Ray-casting does not suffer from these switches and its load can be spread over the GPU threads effectively,

The ray-casting approach also provides previous sample data in a more accessible fashion, which has lead to a technique called *opacity peeling* [26]. In opacity peeling, the ray sampling can skip regions along the view ray (assuming front-to-back traversal). These layers are created when the post-classified opacity  $O$  changes

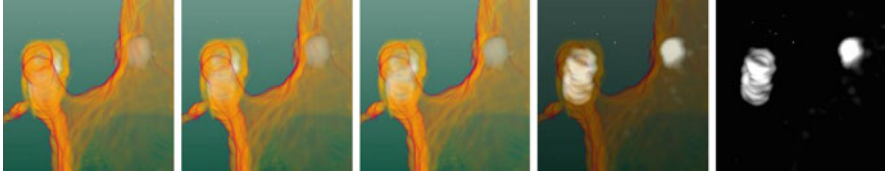


**Fig. 9** Maximum intensity difference accumulation applied to coronary vessels in CT data. From left to right the MIDA control value  $\gamma$  is changed from  $-1$  (left) to  $0$  (center) to  $1$  (right). This is equivalent to blending from DVR to MIDA to MIP. Compared to the original MIDA implementation, the opacity values for MIDA blending were different than for DVR to achieve a higher contrast

( $c = O(s_{i+1}) - O(s_i)$ ) from one sampling point  $s_i$  to another  $s_{i+1}$ . Global or local thresholds can be used to define conditions that represent a layer toggle. For example, in a head CT data the skull can be peeled quickly: The ray will first start out in air, then hit skin and skull both giving  $c \gg 0$ , and finally reach the less dense inner tissue  $c \ll 0$  again. Given this setup, it is easy to completely refine the visual results without segmentation, by specifying which layers shall be made invisible or rendered in a different style.

Bruckner and Gröller [27] introduced the *maximum intensity difference accumulation (MIDA)* to highlight possibly occluded structures. They altered the blending to favor classified samples that have a higher opacity than previous samples. Thus, similar to MIP, high opacity structures are not covered by the accumulation of many low opacity structures. Their  $\gamma$  control value allows a seamless transition from regular DVR to MIDA to MIP (see Fig. 9).

When 1D TFs are used, DVR greatly benefits from pre-integration tables. The quality of the approximation of the volume integral greatly depends on the step width that is used for ray traversal. This especially applies to small vessels when the classification of the vessel wall has other opacities than vessel interior and exterior. Increasing the amount of steps, and therefore lowering the distance between sample points, has a negative impact on the performance of ray-casting. Decreasing the steps, on the other hand, yields aliasing artifacts. However, the pre-integration tables store the integrals between two intensities using a finer sampling. Later at runtime, this pre-computed table  $T$  based on the classification  $C$  only needs to be sampled with front intensity  $s_f$  and back intensity  $s_b$ . The computation of  $T$  is as follows:

$$T(s_f, s_b) = \frac{1}{s_b - s_f} \left( \left( \int_0^{s_b} C(s) ds \right) - \left( \int_0^{s_f} C(s) ds \right) \right). \quad (9)$$

## 5.2 Planar Reformation

In addition to the 3D view, 2D views are crucial in vessel diagnosis. The profile of the vessel wall can give information about narrowings, which can hint at an

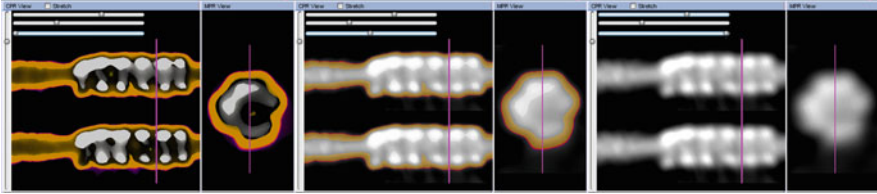


**Fig. 10** Multiplanar reformation of vessels. The vessel viewer shows the opposing longitudinal sections on the left and a planar cross section on the right. Different rendering styles have been used to depict the stent placed inside the arteries. Far left shows isosurface style rendering, whilst far right a classic windowing transfer function. The middle section overlays colored TF with greyscale windowing TF

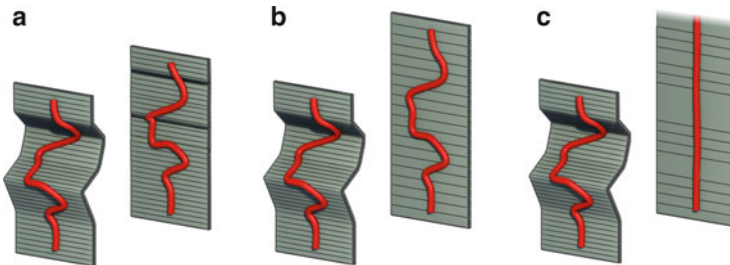


**Fig. 11** Curved Planar Reformation. The unaltered projection perpendicular to the main direction of the vessel may cause overlaps (a). *Stretched* CPR (b) keeps true lengths between vessel path points. *Straight* CPR keeps true lengths and centers path points (c). Image from [30]

undersupply of tissues. Analyzing the vessel's diameter may also reveal signs of calcifications, also known as *plaques* inside the vessel, which also lower blood flow in this area. Wesarg et al. [28] determined vessel diameter changes during the segmentation and also used longitudinal cut views along the vessel's centerline. The cuts were defined by creating a virtual cylinder made of circles perpendicular to the vessel path. When all circles are stacked on top of each other, the vessel is effectively straightened and can be presented in 2D as longitudinal cut through the virtual stacked cylinder (see Fig. 10). To highlight the plaques, arrows are placed in the 3D and 2D views [28].

A similar strategy to depict the vessel along its path is called *curved planar reformation* (CPR). Next to the straightened reformation in 2D, a stretched version has been presented by Kanitsar et al. [29]. The path points are projected perpendicular to the vessel's main direction. When the projection is unaltered, the path can overlap itself and will not be isometric (Fig. 11 A). However, isometry is important for diagnosis, and therefore the following methods are able to provide it. *Stretched* CPR shifts the projected points along the longitudinal axis to account for original lengths between path points. *Straight* CPR eliminates cross-sectional movement, so that the diameter changes of the vessel are easier to read on the longitudinal axis.

Instead of generating a single CPR, the entire vessel tree can be spread into the image plane as well [30]. Iterative relaxation of the outgoing directions at

joint points can assure that vessels do not overlap at branchings. Rotation around the projection plane is still possible, but will mean changes to the position of all subbranches from the root path.

Due to the focus on the vessels in the 2D views, the surrounding context is typically lost. Straka et al. [31] introduced the *vessel glyph* as a set of methods to combine advantages of both 3D and 2D views into a single visualization. They emphasize the vessels, e.g. by fading out or darkening adjacent structures. However, this only works well if the vessels do not exhibit high curvature. Otherwise, they would overlap themselves and create ambiguous images.

### 5.3 Vessel Unfolding

With the increasing resolution of MR and CT scanners, the interior of the vessel may be investigated. Due to the similarity of the geometry to much larger structures such as the colon, some techniques developed for the colon wall visualization can be adapted to the smaller vessels. One such technique is *virtual colon unfolding* [32]. It creates a 2D image of the entire colon wall. In a recent work, Ropinski et al. [33] used vessel unfolding and flattening to reveal measured data within the vessels. They have also aligned the unfolded structures to simplify comparison between different datasets.

Due to the aforementioned progress in scanning quality, it is expected that other visualization methods make this transition, e.g. virtual endoscopy turning into virtual angiography. Further reduction in noise and improved image resolution with more voxels shall also improve the output of histogram-based visualization methods (see Sect. 6.2, Fig. 17).

## 6 Case Studies

We have presented several basic and advanced DVR techniques to display vessel structures. In the following case studies, we will present two techniques that were customized to specific diagnostic tasks. The first is a simplified filtering technique for implicit segmentation of the main cerebral vessels, which provide context to simulation meshes. The second provides a refined local histogram analysis to create TFs, which highlight pathologies for diagnosis of the coronary artery disease (CAD).

## 6.1 Case Study 1: DVR of Cerebral Vasculature in MRA Data

Cerebral aneurysms develop from a congenital or acquired weakness of stabilizing parts of the cerebral arterial vessel wall. They bear a higher tendency of rupture, with often fatal consequences for the patient. To gain insight into the cause and evolution of cerebral aneurysms and to reduce the risk of surgical or endovascular treatment [34], a detailed characterization of morphology (size, shape), morphodynamic (pulsatile change of morphology), and hemodynamics (blood flow pattern) is important [35]. Neugebauer et al. [36] focus on the evaluation of the morphology with focus-and-context rendering. They propose a hybrid rendering: a polygonal representation of the mesh containing the flow data and a volume rendering of the contextual vasculature. A filtering is necessary to ensure that only relevant information are included into the volume rendering. In contrast to the complex filtering kernels mentioned in Sect. 3.3, they suggested a simpler series of image processing operations to detect vessels surrounding a cerebral aneurysm. As input, MR-Time of Flight (TOF) data is used. Due to a special setup, the TOF sequences yield a high signal from blood moving into the direction of the slice plane's normal (see Fig. 12c). By exploring ten datasets with varying intensity values and from different scanner devices, they have empirically created the following workflow (Fig. 13):

1. *Binary threshold.* Due to the high intensity values of vessels in MRA-TOF data, a simple threshold operation removes most of the disturbing data. The intensity histograms of the datasets are analyzed for common characteristics to determine a proper threshold. Because of individual varyings between datasets, the threshold is based on the equalized histogram, which compensates for image intensities and overall contrast between vessels and tissue. The mean value position  $p$  in the equalized image histogram is used to define the refined threshold as  $T = p \cdot 0.5$ , which is found to be close to  $I_{max} \cdot 0.25$ . After applying the threshold, the image contains all the arteries of interest, but also parts of high intensity brain tissue and skin, as well as some noise (see Fig. 13b).
2. *Connected component analysis.* Voxels belonging to arteries form large groups, whereas skin and tissue-related voxels split up into several small groups (see Fig. 13b). This observation motivated the use of a connected component analysis to distinguish between relevant (arteries) and irrelevant (skin, tissue) structures. In the following, the voxel-groups are referred to as components. The noise is removed by discarding all components smaller than 0.01% (empiric threshold) of the overall dataset volume. The components left are the main cerebral arteries and parts of the skin. Removal of the skin components is achieved by taking into account that the arteries are located along the center medial axis of the head (see Fig. 13c). The bounding boxes of all components are projected into the *transverse plane* (medical term). Since the arteries are close to the center and run mostly vertically, their bounding box centers  $c$  are clustered in this plane. In contrast, the skin components exhibit a lower clustering rate. The closest center to the heads vertical axis becomes the reference origin  $o$ . The distances  $d_i = |c_i - o|$  of all bounding box centers are calculated relative to  $o$  and sorted



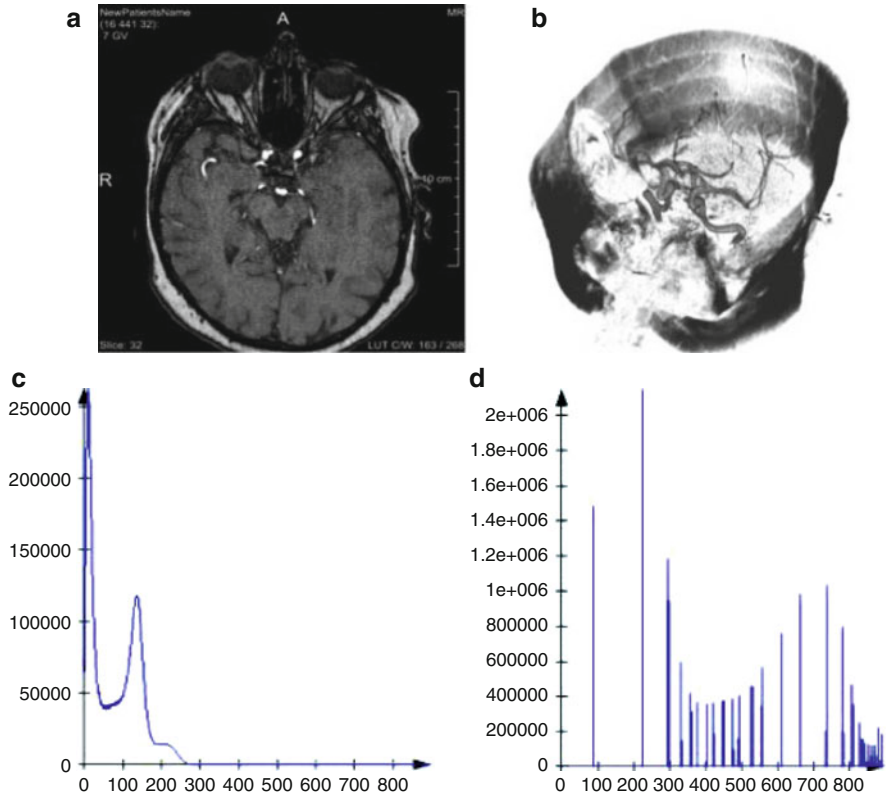


**Fig. 12** Analysis of the dataset's intensity values: slice view (a), volume view (b), histogram (c), equalized histogram (d). The vessel and skin intensity values are within the upper half of the equalized histogram

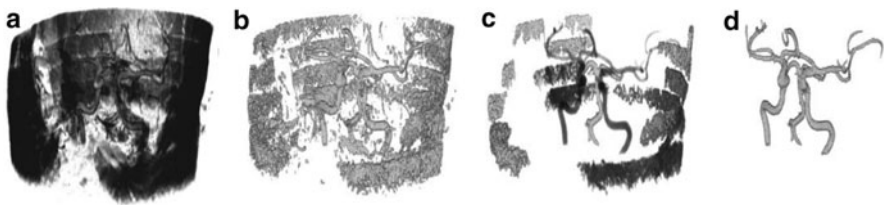


**Fig. 13** The different stages of the filtering processes: original data (a), threshold applied (b), connected component analysis discarding small structures (c), removal of outer skin structures (d)

in ascending order. By sorting the distances, the aforementioned axial-center distance is included in all following calculations. Based on the ordered distance list, the mean  $m$  value of the distance intervals  $D_i = d_{i+1} - d_i$  is calculated. This mean value is a simplified measure to identify a spatial clustering, the second of

the aforementioned characteristics are utilized to distinguish between skin and arteries. All components that belong to an interval  $D_i < m \cdot b$ , are defined as components that represent arteries. Experiments on several datasets have shown that  $b = 1.2$  is an adequate choice to describe the common cluster density of components belonging to cerebral arteries (see Fig. 13d). The parameter  $b$  describes the relative rate of distance-change and is therefore invariant with respect to resolution and size of the dataset.

3. *Proximity-based preservation of details.* Whereas the large arteries can be filtered in a robust manner by the connected component analysis, small vessels that potentially emanate from the aneurysm body, cannot be filtered explicitly. They have a small diameter ( $\approx 2-3$  voxels), are often fragmented because of insufficient spatial resolution of the MR scan and exhibit low contrast differences with respect to the surrounding tissue due to the high relative impact of the partial volume effect. Thus, those vessels exhibit characteristics similar to noise, tissue and skin artifacts, and are consequently removed during the connected component analysis. Despite the vague representation, these small vessels are diagnostically important and should be included in the context visualization. An experienced radiologist is able to visually distinguish between noise and small vessels, if the view at the region containing the small vessels is not occluded. Hence, the region near the aneurysm is included in the context visualization. This region is chosen by proximity without any filtering. A smooth reduction of intensity with increasing distance to the aneurysm surface is applied to reduce the rate of occlusion. This is possible since the opacity of the rendered voxels will be linked to their intensity when the transfer function is applied within the final visualization.

A weighted volume mask is created with an Euclidian distance transform (EDT) to show possible vessels near the voxelized aneurysm. It is crucial that the polygonal simulation mesh is registered properly with the volume data, so that its voxelisation matches the volume dataset. This should be taken into account when generating the original mesh. The distance field  $F$  is the result of the EDT and encodes scalar values between 0 and 1, where 0 describes the minimal distance to the aneurysm surface, and 1 is the maximum distance found at the border of the dataset. To create a smooth ramp mask covering the local surrounding of the aneurysm, first,  $F$  is inverted and then a rescaled distance field  $F'$  generated with:

$$F' = \max(0, (\text{inv}(F)1 + (1/c)) \cdot c), \quad (10)$$

whereas  $c$  is a constant. For all datasets,  $c = 10$  led to a well-sized ramp mask for the local aneurysm surrounding.

4. *Final Mask Creation.* The result of the connected component analysis is a binary volume, on which a morphological dilation filter with a  $3 \times 3 \times 3$  kernel is applied. Thus, it is ensured that the vessel surface is represented completely when masking the original data, as partial volume effect mainly affects the intensities of border voxels between vessel and surrounding tissue. This mask is combined with the EDT mask by applying the arithmetic image operation  $\max$ . The result is a mask that will preserve the main arteries and low contrast information near

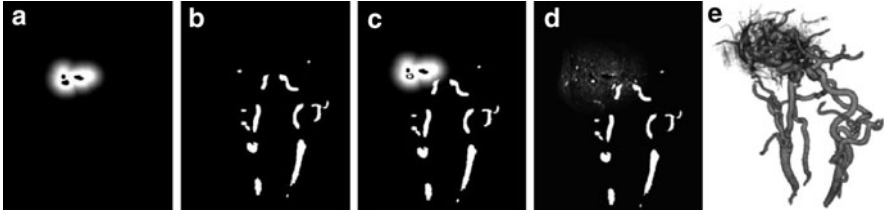


**Fig. 14** To show small vessels surrounding the aneurysm, a weighted distance field (a) is generated from its voxelization. The mask is a combination of the main vessels (b) and the distance field using a maximum operator (c). Finally, it is weighted by volumes original intensity values (d) and used in the 3D view (e)

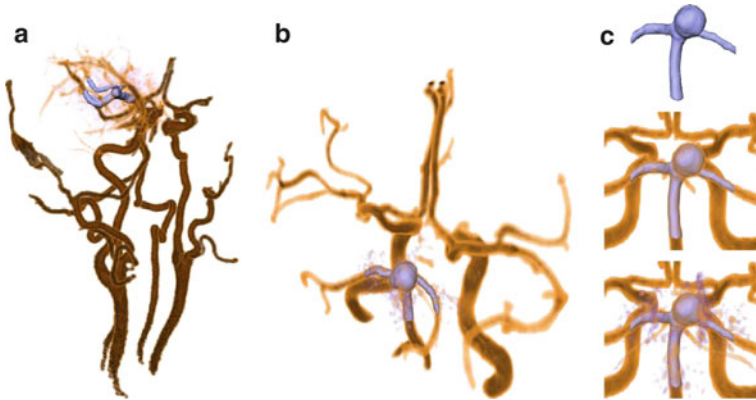


**Fig. 15** The focus-and-context visualization shows both the polygonal simulation mesh and surrounding vessels via hybrid rendering. (a) and (b) show different 1D-transfer functions. The last image series illustrates the benefits of additional context information, and makes use of a grow distance field to reveal small vessels coming from the aneurysm

to the aneurysm surface, when multiplied with the original dataset (see Fig. 14d). In order to create this mask automatically, two defined constants are utilized:  $b$  and  $c$ . Both are independent variables and exhibit robust characteristics (for the tested datasets: stable results when altered  $\pm 20\%$ ).

With the use of 1D TFs the final visualization is presented in Fig. 15. Hybrid rendering was used to integrate the polygonal simulation mesh into the final scene. To avoid artifacts around the mesh, its voxelized version was subtracted from the original volume data to avoid double representation of the same structure.

## 6.2 Case Study 2: Emphasis of Plaques in Coronary Arteries

In the second example, we present a local histogram-based approach to highlight atherosclerotic CAD. Atherosclerotic CAD is the result of accumulations in the

coronary artery wall, so-called plaques. Plaque deposits are small structures with inhomogeneous densities inside the vessel wall and cannot be segmented directly in CT angiography (CTA) datasets. Therefore, a DVR visualization of the coronary artery tree should highlight the vessel wall and emphasize coronary artery plaques in CTA datasets by employing special TFs. Glasser et al. [37] developed a TF specification for DVR visualizations of the coronary arteries in CTA datasets. The TFs are automatically adapted to each dataset to account for varying CT values of the blood pool, due to the non-uniform spatial diffusion of the contrast agent. The presented workflow for TF specification is based on a coarse segmentation of the coronary artery tree including the segmentation's skeleton and contains the following steps:

1. *Approximation of the blood density values.* The segmented coronary artery tree primarily consists of voxels representing the contrast medium-enhanced blood and is analyzed for the approximation of the blood density distribution. The blood density is assumed to be a Gaussian distribution with parameters  $\mu_{blood}$  and  $\sigma_{blood}$ . Because of other densities originating from surrounding tissue or interpolation issues, i.e. the partial volume effect,  $\mu_{blood}$  and  $\sigma_{blood}$  could not be directly derived from the segmentation. Therefore, the approximation is carried out by means of an iterative reduction of a cost function. Costs are defined as differences between the approximated normal distribution and the distribution of all segmented voxels. The mean density of the blood (i.e.  $\mu_{blood}$  and  $\sigma_{blood}$ ) strongly differs for each dataset [37]. Therefore, a static threshold for a separation of hard plaques from blood was not applicable. Instead, a threshold  $t$ , similar to the threshold of the Agatston score [38], was introduced. To avoid overestimation,  $t$  is defined as

$$t = \mu_{blood} + 3\sigma_{blood}. \quad (11)$$

2. *Approximation of the vessel wall density values.* The approximation of the vessel wall density values is based on the evaluation of a coronary artery segment and its skeleton. The vessel wall of this segment is analyzed by means of intensity profile volumes (IPV), as described in [37]. The IPV calculation is carried out in four steps (see Fig. 16, left):
  - a. Selection of a long, non-branching segment of the coronary artery tree. The selection is carried out by traversing the skeleton of the segmentation.
  - b. The real vessel centerline is approximated by the segment skeleton.
  - c. For each skeleton voxel,  $n$  rays perpendicular to the skeleton are casted.
  - d. Along the rays, intensities are sampled and saved in a slice of the IPV.

After the IPV extraction, the vessel wall densities can be approximated. For each skeleton voxel, the sampled intensities representing the vessel wall will appear as vertical structures in a slice of the IPV (see Fig. 16, right). The IPV is slicewise convoluted with a Gaussian and a Sobel filter by applying a 2D filter to each slice. The convolutions are followed by a search for vertical structures

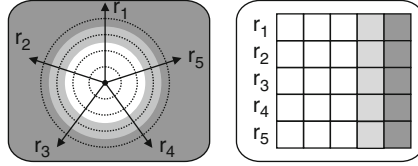


**Fig. 16** Extraction of a slice of the intensity profile volume (IPV). For each voxel  $v$  of the skeleton of a vessel segment,  $n$  (e.g. 5) rays perpendicular to the centerline are casted (left). Along the rays, intensities are sampled and saved in a slice of the IPV (right). A cross-section of an ideal vessel (white) and the vessel wall (light gray) with surrounding tissue (dark gray) leads to vertical structures in the IPV slice for  $v$ . The IPV has as many slices as the number of centerline voxels

to obtain a sample set of vessel wall intensities. This sample comprises a set of intensities  $d_i$ , where a weight  $w_i$  is assigned to each  $d_i$ , see also [37]. Based on this sample,  $\mu_{wall}$  and  $\sigma_{wall}$  are computed as weighted arithmetic mean and weighted arithmetic standard deviation, respectively:

$$\mu_{wall} = \frac{\sum w_i * d_i}{\sum w_i} \quad (12)$$

$$\sigma_{wall} = \sqrt{\sum w_i^2 * \sigma_i^2}, \quad (13)$$

where  $\sigma_i$  is the standard deviation for each density  $d_i$ .

3. *TF specification and DVR visualizations.* For the visualizations of the CTA datasets,  $TF_{2D}$  and  $TF_{3D}$  were determined for 2D and 3D visualizations. They solely depend on  $\mu_{blood}$ ,  $\sigma_{blood}$ ,  $\mu_{wall}$  and  $\sigma_{wall}$  and differ only in the interval size of the vessel wall densities. An interval of  $\mu_{wall} \pm \sigma_{wall}$  is employed for the  $TF_{3D}$ , and an interval  $\mu_{wall} \pm 2\sigma_{wall}$  for the  $TF_{2D}$ . This choice is motivated by a possible occlusion of inner structures within the vessel wall in 3D visualizations. Therefore, also smaller opacity values for the vessel wall are assigned for the  $TF_{3D}$  than for the  $TF_{2D}$ . In comparison, the vessel wall and hard plaques are mapped to higher opacity values, whereas absolute transparency is assigned to the surrounding tissue and the contrast medium-enhanced blood.

A color scale from blue over red to green provides high contrasts for the visualization of different plaque deposits and thus different densities in the vessel wall. For hard plaques, the assigned colors range from beige to white, since these structures usually appear white or light gray in conventional CT displays. For a more intuitive view, the  $TF_{2D}$  is combined with the windowing TF. The user can choose interesting HU value intervals by manipulating the parameters of the windowing TF. The CPR and MPR view as well as the 3D spatial variation of the coronary artery tree are linked with each other. On the one hand, the user can traverse the CPR view with the corresponding MPR view being updated. On the other hand, it is possible to pick an interesting vessel part in the 3D view with the other views being updated accordingly.

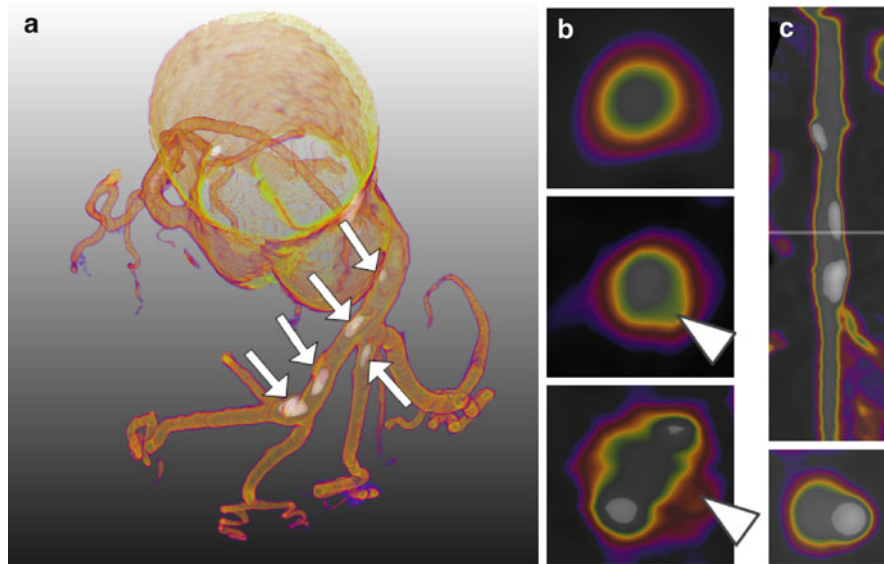


**Fig. 17** Visualizations of coronary arteries with adapted TFs. (a) DVR visualization provides an overview about the spatial variation and of hard plaques (arrows). (b) MRP views provide cross-sectional views of the coronary artery walls. The type of plaque (arrowheads) may be inferred from the color coding: MRP view without plaques (top), greenish colors indicate fibrous plaques (middle) and pinkish colors indicate soft plaques, which are prone to rupture (bottom). (c) shows the combined CPR-MPR view. The transparent white bar indicates the current position in the CPR view (top) of the cross-sectional MPR view (bottom)

Discussions with two experienced radiologist indicate that the presented TFs highlight stenotic plaque deposits, and display smaller plaques without a significant stenosis. The 3D visualizations show the spatial variation of the coronary artery tree and indicate the patient's whole plaque burden by highlighting all hard plaques (see Fig. 17a). In the combined CPR-MPR view, the plaques are highlighted with different colors depending on the plaque type (see Fig. 17b). Comparisons between conventional views and the  $TF_{2D}$  and  $TF_{3D}$  color-coded visualizations indicate that the clinical expert can better detect hard plaques in the colored view. Especially smaller hard plaques, even with a size of one voxel, could be detected in the colored view. Furthermore, the color coding of the vessel wall with different colors for fibrous and soft plaque deposits indicates the plaque type, where an absolute identification is impossible due to overlapping density intervals of these types [39].

## 7 Concluding Remarks

The visualization of vascular structures is challenging due to their small size and complex topology. Various DVR techniques have been successfully employed to deal with these demands. The quality of vessel visualization benefits from pre-processing and filtering, which highlight elongated circular structures (vesselness). A histogram-based TF specification is particularly useful, when applied to local histograms, e.g. of segmented vessels. For a vessel disease diagnosis system (e.g. Vascu Vision by Boskamp et al. [40]) the combination of 2D and 3D views is essential, as only their combination can reveal the adequate detail (e.g. cross-sectional and longitudinal views to access the vessel's diameter and wall) and overview information (e.g. the patient individual spatial variation). In principle, automatically generated visualizations and an analysis of changes in the local vessel diameter might be used to emphasize potentially portions (see [28] for such attempts in cardiology). Compared to surface-based techniques, DVR may also display important changes of the vessel wall and not only its general shape. Preprocessing and detailed analysis of the data can help to create a customized workflow. To support diagnostic tasks, fast, reliable, and easy to setup techniques are favorable for clinical routine, but accuracy or visualization of uncertainty must not be compromised.

### 7.1 Future Work

The rising availability of memory and performance in consumer hardware, e.g. in many-core systems such as GPUs and future computing devices, will continue to aid volume analysis to enhance vessel exploration with DVR. However, not only analysis but also the rendering itself leaves room for improvements, especially when it comes to simulating advanced optical effects. Advanced illumination techniques, such as ambient occlusion (see Fig. 18 left), can improve the depth perception. Especially when many small vessels and many branchings exist, the structures may overlap each other extensively in a 2D image. Therefore, custom shading methods can give more clues about the spatial relationship among vessels and/or context structures. Other optical effects, like more sophisticated scattering and shadowing models, also raise the possibilities for visualizations (see Fig. 18 right, [41]). The major problem of these techniques remains complexity in time or resources, which limits them to high-end graphics cards or sacrificing interactivity. However, both technical and algorithmic advances continue to improve the situation in visual computing and future technology trends, such as cloud computing, will enhance the end-user experience.



**Fig. 18** Advanced illumination techniques. The left images shows parts of cerebral vessels. Through the use of self-shadowing, the geometric relationship between vessels is enhanced and fine-dotted lines show the occluded silhouettes. The flat planes at various branching points are the result of a limited region-of-interest. In the right advanced soft shadowing techniques were used on coronary vessels. (Right image taken from [41])

**Acknowledgements** The case studies were contributed to by O. Beuing, V. Diehl, R. Gasteiger, A. Mahnken, S. Oeltze and S. Wilhelmssen. We thank Dr. S. Achenbach (University of Erlangen-Nürnberg, Germany) for providing the coronary vessel CT image data and Fraunhofer MEVIS for providing advanced MeVisLab features. We thank P. Hastreiter, A. Joshi, S. Wesarg, A. Kanitsar and T. Ropinski for allowing us to use images from their publications and S. Quade and P. Greveson for their input.

## References

1. Preim B, Oeltze S. Visualization in Medicine and Life Sciences. In: Linsen L, Hagen H, editors. 3D Visualization of Vasculature: An Overview. Springer Verlag; 2007. 19–39.
2. Selle D, Preim B, Schenk A, Heinz-Otto-Peitgen. Analysis of Vasculature for Liver Surgery Planning. *IEEE Transactions on Medical Imaging*. 2002 November;21(11):1344–1357.
3. Zerfowski D. Motion artifact compensation in CT. In: *SPIE Medical Imaging 1998: Image Processing*; 1998. p. 416–424.
4. Zheng L, Maksimov D, Stutzmann T. Bone removal in dual energy CT. In: *CVII 2008: Computer Vision for Intravascular and Intracardiac Imaging*; 2008. 120–127.
5. Blum H. Biological shape and visual science: Part I. *J Theor Biology*. 1973;38:205–283.
6. Sethian JA. *Level Set Methods and Fast Marching Methods: Evolving Interfaces in Computational Geometry, Fluid Mechanics, Computer Vision, and Materials Science*. 2nd ed. Cambridge University Press; 1999.
7. Schaap M, Metz CT, van Walsum T, van der Giessen AG, Weustink AC, Mollet NRA, et al. Standardized Evaluation Methodology and Reference Database for Evaluating Coronary Artery Centerline Extraction Algorithms. *Medical Image Analysis*. 2009;13/5:701–714.
8. Boskamp T, Hahn H, Hindennach M, Zidowitz S, Oeltze S, Preim B, et al. Geometrical and Structural Analysis of Vessel Systems in 3D Medical Image Datasets. In: Leondes CT, editor. *Medical Imaging Systems: Technology und Applications*. vol. V. World Scientific Press; 2005. 1–60.
9. Kanitsar A, Wegenkittl R, Felkel P, Fleischmann D, Sandner D, Gröler E. Computed Tomography Angiography: A Case Study of Peripheral Vessel Investigation. In: *IEEE Visualization*; 2001. 477–480.



10. Frangi AF, Frangi RF, Niessen WJ, Vincken KL, Viergever MA. Multiscale Vessel Enhancement Filtering. Springer-Verlag; 1998. 130–137.
11. Joshi A, Qian X, Dione D, Bulsara K, Breuer C, Sinusas A, et al. Effective visualization of complex vascular structures using a non-parametric vessel detection method. *IEEE Transactions on Visualization and Computer Graphics*. 2008;14(6):1603–1610.
12. Kindlmann G, Durkin JW. Semi-automatic generation of transfer functions for direct volume rendering. In: *IEEE Symposium on Volume Visualization*; 1998. 79–86.
13. Kniss J, Kindlmann G, Hansen C. Multidimensional Transfer Functions for Interactive Volume Rendering. *IEEE Transactions on Visualization and Computer Graphics*. 2002;8(3):270–285.
14. Vega Higuera F, Sauber N, Tomandl B, Nimsky C, Greiner G, Hastreiter P. Enhanced 3D-Visualization of Intracranial Aneurysms Involving the Skull Base. In: *MICCAI (2)*; 2003. 256–263.
15. Rezk-Salama C, Hastreiter P, Scherer J, Greiner G. Automatic Adjustment of Transfer Functions for 3D Volume Visualization. In: *VMV*; 2000. 357–364.
16. Vega Higuera F, Sauber N, Tomandl B, Nimsky C, Greiner G, Hastreiter P. Automatic adjustment of bidimensional transfer functions for direct volume visualization of intracranial aneurysms. In: *Proc. of Society of Photo-Optical Instrumentation Engineers (SPIE)*. vol. 5367; 2004. 275–284.
17. Lundström C, Ljung P, Ynnerman A. Local Histograms for Design of Transfer Functions in Direct Volume Rendering. *IEEE Transactions on Visualization and Computer Graphics*. 2006;12(6):1570–1579.
18. Lundström C, Ljung P, Persson A, Ynnerman A. Uncertainty Visualization in Medical Volume Rendering Using Probabilistic Animation. *IEEE Transactions on Visualization and Computer Graphics*. 2007;13(6):1648–1655.
19. Tappenbeck A, Preim B, Dicken V. Distance-Based Transfer Function Design: Specification Methods and Applications. In: *Simulation und Visualisierung*; 2006. 259–274.
20. Correa CD, Ma KL. Size-based Transfer Functions: A New Volume Exploration Technique. *IEEE Transactions on Visualization and Computer Graphics*. 2008;14(6):1380–1387.
21. Kanitsar A, Fleischmann D, Wegenkittl R, Gröller ME. Diagnostic Relevant Visualization of Vascular Structures. Favoritenstrasse 9-11/186, A-1040 Vienna, Austria; 2004. Human contact: technical-report@cg.tuwien.ac.at.
22. Zuiderveld KJ, Koning AHJ, Viergever MA. Techniques for speeding up high-quality perspective maximum intensity projection. *Pattern Recogn Lett*. 1994;15(5):507–517.
23. Sato Y, NSTS Shiraga N, R K. LMIP: Local Maximum Intensity Projection: Comparison of Visualization Methods Using Abdominal CT Angiography. *Journal of Computer Assisted Tomography*. 1998;22(6):912–917.
24. Scharsach H, Hadwiger M, Neubauer A, Wolfsberger S, Bühler K. Perspective Isosurface and Direct Volume Rendering for Virtual Endoscopy Applications. In: *EG/IEEE Eurovis*; 2006. 315–322.
25. Vega Higuera F, Hastreiter P, Fahlbusch R, Greiner G. High Performance Volume Splatting for Visualization of Neurovascular Data. In: *IEEE Visualization*; 2005. 35–42.
26. Rezk-Salama C, Kolb A. Opacity Peeling for Direct Volume Rendering. *Computer Graphics Forum (Proc Eurographics)*. 2006;25(3):597–606.
27. Bruckner S, Gröller ME. Instant Volume Visualization using Maximum Intensity Difference Accumulation. *Comput Graph Forum*. 2009;28(3):775–782.
28. Wesarg S, Khan MF, Firlle E. Localizing Calcifications in Cardiac CT Data Sets Using a New Vessel Segmentation Approach. *J Digital Imaging*. 2006;19(3):249–257.
29. Kanitsar A, Fleischmann D, Wegenkittl R, Felkel P, Gröller ME. CPR: curved planar reformation. In: *IEEE Visualization*; 2002. 37–44.
30. Kanitsar A, Wegenkittl R, Fleischmann D, Grolller ME. Advanced Curved Planar Reformation: Flattening of Vascular Structures. In: *IEEE Visualization*; 2003. 43–50.
31. Straka M, Cervenansky M, La Cruz A, Kochl A, Sramek M, Grolller E, et al. The VesselGlyph: Focus & Context Visualization in CT-Angiography. In: *IEEE Visualization*; 2004. 385–392.

32. Bartrolí AV, Wegenkittl R, König A, Gröller E. Nonlinear virtual colon unfolding. In: IEEE Visualization; 2001. 411–420.
33. Ropinski T, Hermann S, Reich R, Schäfers M, Hinrichs KH. Multimodal Vessel Visualization of Mouse Aorta PET/CT Scans. IEEE Transactions on Visualization and Computer Graphics (TVCG) (Vis Conference Issue). 2009; 1515–1522.
34. Anxionnat R, Bracard S, Ducrocq X, Troussset Y, Launay L, Kerrien E, et al. Intracranial Aneurysms: Clinical Value of 3D Digital Subtraction Angiography in the Therapeutic Decision and Endovascular Treatment. Radiology. 2001; 799–808. Article dans revue scientifique avec comité de lecture.
35. Zhan C, Villa-Uriol MC, Craene MD, Pozo JM, Frangi AF. Morphodynamic Analysis of Cerebral Aneurysm Pulsation from Time-Resolved Rotational Angiography. MedImg. 2009 July;28(7):1105 – 1116.
36. Neugebauer M, Gasteiger R, Diehl V, Beuing O, Preim B. Automatic generation of context visualizations for cerebral aneurysms from MRA datasets. International Journal of Computer Assisted Radiology and Surgery (CARS). 2009 Juni;4 (Supplement 1):112–113.
37. Glaßer S, Oeltze S, Hennemuth A, Kubisch C, Mahnken A, Wilhelmsen S, et al. Automatic Transfer Function Specification for Visual Emphasis of Coronary Artery Plaque. Computer Graphics Forum. 2010;29(1):191–201.
38. Agatston AS, Janowitz WR, Hildner FJ, et al. Quantification of coronary artery calcium using ultrafast computed tomography. J Am Coll Cardiol. 1990;15(4):827–832.
39. Pohle K, Achenbach S, MacNeill B, et al. Characterization of non-calcified coronary atherosclerotic plaque by multi-detector row CT: Comparison to IVUS. Atherosclerosis. 2007;190:174–180.
40. Boskamp T, Rinck D, Link F, Kmmmerlen B, Stamm G, Mildenerger P. New Vessel Analysis Tool for Morphometric Quantification and Visualization of Vessels in CT and MR Imaging Data Sets. Radiographics. 2004;24(1):287–297.
41. Ropinski T, Döring C, Rezk-Salama C. Advanced Volume Illumination with Unconstrained Light Source Positioning. IEEE Computer Graphics and Applications. 2010; Accepted for publication.